Electronic Supplementary Material (ESI) for Nanoscale.
This journal is © The Royal Society of Chemistry 2021

Supporting Information

Transformation from Non-radical to Radical Pathway by Amorphization of $Ni(OH)_2$ Catalyst as Peroxymonosulfate Activator for Ultrafast Degradation of Organic Pollutants

Hui Wang,[a] Wenwen Xu,[a] Xu Chen,[a] Qihao Yang,[a] Cai Shen,[a,b] Baoshan Zhang,[a] Yichao Lin,[a,b] Jian Sun,[c] Linjuan Zhang,[*c] Qiuju Zhang,[*a,b] Zhiyi Lu[*ab] and Liang Chen[a,b]

[a] Ningbo Institute of Materials Technology & Engineering Chinese Academy of Sciences, Ningbo 315201, People's Republic of China

[b] University of Chinese Academy of Sciences, Beijing 100049, People's Republic of China

[c] Key Laboratory of Interfacial Physics and Technology, Shanghai Institute of Applied Physics, Chinese Academy of Sciences, Shanghai 201800, People's Republic of China

[*]Correspondence to: zhanglinjuan@sinap.ac.cn (L. Zhang), zhangqj@nimte.ac.cn (Q. Zhang) and luzhiyi@nimte.ac.cn (Z. Lu).

This supporting information contains:

Supplementary Figures S1-S17.

Supplementary Tables S1-S3.

Supplementary References.

Methods

Chemicals.

Nickel nitrate, sodium nitrate, sodium sulfite, formamide and methanol were purchased from Sinopharm Chemical Reagent Co., Ltd. Sodium hydroxide, rhodamine B (RhB), bisphenol A (BPA), *p*-chlorophenol (4-CP) Tert-butanol (TBA), 5,5-dimethyl-1-pyrroline N-oxide (DMPO) and 4-hydroxy-2,2,6,6-tetramethylpiperidine (TEMP) were obtained from Aladdin Co., Ltd. Peroxymonosulfate ($KHSO_5 \cdot 0.5KHSO_4 \cdot 0.5K_2SO_4$) was achieved from Sigma-Aldrich. All chemical reagents were directly used without purification.

Characterization.

The sample of A-$Ni(OH)_2$ was lyophilized by vacuum freeze-drying apparatus (Foring Technology LGJ-10C) at least 24 h before characterization. The structure and morphology of the catalysts are characterized by X-ray diffraction (XRD, BrukerD8 ADVANCE) equipped with Cu Kα radiation, field-emission scanning electron microscopy (SEM, Hitachi S4800) and atomic force microscope (AFM, Bruker, Dimension Icon). Transmission electron microscopy (TEM) and corresponding element mapping images were performed on a FEI Tecnai G2 F20 electron microscope. X-ray photoelectron spectra (XPS) was carried out on a Thermo SCIENTIFIC ESCALAB 250Xi spectrometer with Al Kαas the excitation source. Fourier transform infrared reflectance (FTIR) spectra of samples were obtained on a ThermoFisher NICOLET 6700 spectrometer. Raman analysis was acquired on a Renishaw InVia Reflex spectrometer with a green light of an N_d-YAG laser (532 nm). Ni K-edge X-ray absorption spectroscopy (XAS) were conducted at beamline 14W1 of the Shanghai Synchrotron Radiation Facility (SSRF), China and XAFCA beamline of Singapore Synchrotron Light Source. Data were recorded in transmission mode for Ni K-edge. All XAFS data were analyzed using the program Demeter.[1] For all samples, the EXAFS oscillations were extracted from the normalized XAS spectra by subtracting the atomic background using a cubic spline fit to k^3-weighted data, where k is the photoelectron wave number. The $\chi(k)$

functions were then Fourier transformed into R-space. The Fourier-transform window was in the *k* range 2–12 Å for Ni.

Catalytic activity performance evaluation.

Here, a mass-based degradation rate (v, μmol s^{-1} g^{-1}) was employed to evaluating the PMS catalytic activity by various catalysts as eq S1 shows.

$$v=\frac{1}{m}\times\frac{dn}{dt} \tag{S1}$$

Where m is the mass of catalyst (g), n is the amount of degraded organic contaminant (μmol) and t is the reaction time (s).

The reaction rate constant of RhB degradation was evaluated by a pseudo first-order kinetics model (eq S2).

$$\ln\left(C_0/C_t\right)=kt \tag{S2}$$

Where C_0 and C_t (mg/L) are the initial contaminant concentration and concentration at a certain time t (min) during the PMS activation process and k (min^{-1}) is the reaction rate constant.

Quenching experiment: Screen radical experiment was performed to quantify the contribution of various radicals to the degradation efficiency of RhB. TBA (radical scavenger for $^{\bullet}OH$, 1.0 M) and MeOH (radical scavenger for both $^{\bullet}OH$ and $SO_4^{\bullet-}$, 1.0 M) was added into the PMS activation reaction after 30 min adsorption. Then, the samples were withdrawn at intervals for further analysis.

The degradation intermediates of RhB were identified using AB SCIEX (TripleTOF 4600) liquid chromatography–quadrupole time-of-flight mass spectrometry (QTOF/MS/MS) system. The chromatographic separations were carried out on a HSS T3 column (1.8 μm, 2.1×100 mm). Gradient elution was employed in the test and the mobile phase consisted of water with 0.1% formic acid (eluent A) and methanol with 0.1% formic acid (eluent B), the sample injection volume was 10 μL.

The electron paramagnetic resonance (EPR) spectra were employed to identify reactive

oxidative species (ROS) involved in the PMS/$Ni(OH)_2$ system. DMPO was used as the spin trap agent for both $^{\bullet}OH$ and $SO_4^{\bullet-}$ in water and $O_2^{\bullet-}$ in methanol, respectively. The detection of $^1O_2$ was conducted employing TEMP as the spin trapping agent. For typical testing, 0.05 g/L catalyst and 0.15 g/L PMS was mixed in water, then DMPO (250 mM) was added to trap $^{\bullet}OH$ and $SO_4^{\bullet-}$. When the dosage of catalyst was increased to 0.20 g/L under the same condition, DMPO was directly oxidized into DMPOX (**Figure S12**). 0.20 g/L catalyst and 0.15 g/L PMS was mixed in methanol, then DMPO (250 mM) was added to trap $O_2^{\bullet-}$. 0.20 g/L catalyst and 0.15 g/L PMS was mixed in water, then TEMP (100 mM) was added to trap $^1O_2$. The obtained solution was immediately inserted into the cavity of the EPR equipment, after addition of spin trap agent. The spectra were obtained by a Bruker E500 spectrometer with a center field at 3505 G at room temperature.

Electrochemical measurement: In a typical electrode test system, a carbon rod and saturated calomel electrode (SCE) were used as the counter and reference electrodes, respectively. A fresh polished glassy carbon (Pine Research Instrumentation HTW GmbH, 0.247 cm^{-2}) was used as the working electrode substrate and the electrolyte was 0.1 M KOH. 1.0 mg C-$Ni(OH)_2$ sample was added into 1 mL absolute ethanol. For A-$Ni(OH)_2$, 1.0 g/L colloid sample was prepared by using ethanol instead of water. Then, 3mg conductive carbon (Super P, Alfa Aesar) and 0.05 mL Nafion solution (5 wt%, Sigma-Aldrich) were added into the catalyst ethanol solution. After the sonication process for 30 min, 10 μL of the as-prepared catalyst ink was pipetted onto the surface of the glassy carbon electrode. The catalyst layer was dried in ambient air before testing. All the electrochemical data were recorded on a CHI 760E bipotentiostat. Cyclic voltammetry (CV) measurement was performed with glassy carbon rotating rate of 1600 rpm between 0~0.65 V *vs*. SCE at a scan rate of 10 mV s^{-1}.

Computational details and models

Spin-polarized density functional theory (DFT)[2] was conducted in the Vienna ab initio simulation package (VASP).[3] We adopt the projected augmented-wave method (PAW)[4]

potentials, and the exchange–correlation energy of the general gradient approximation (GGA) in the scheme proposed by Perdew–Burke–Ernzerh (PBE).[5] The cut-off kinetic energies for the plane waves were set to 480 eV for all the calculations. The convergence tolerance of energy and force on each atom during structure relaxation are less than 10^{-4} eV and 0.02 eV $Å^{-1}$. A set of Gamma meshed K points of were used to sample the Brillouin zone for geometry optimization and electronic structural calculations of $Ni(OH)_2$ supercells.[6] The *c* axis was set to 15 Å for C-$Ni(OH)_2$ surface to ensure sufficient vacuum to avoid interactions between two periods. The amorphous model was built by removing the −OH bond to distort C-$Ni(OH)_2$, as shown in **Figure S13**. The removing of two −OH groups produces a hole to expose the active Ni site, which is used to simulate the defect Ni sites or edge Ni sites in amorphous state. Vibrational frequencies were also calculated to verify the obtained transition structures, using the dynamic matrix method.[7]

(a)

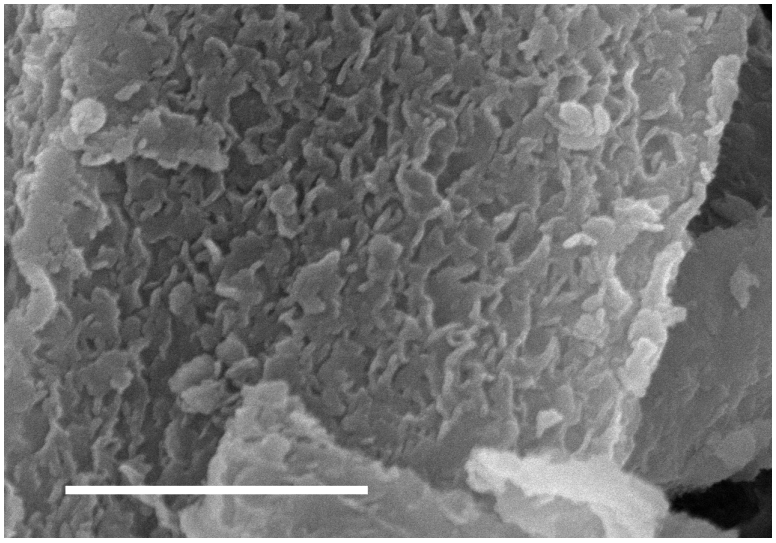

(b)

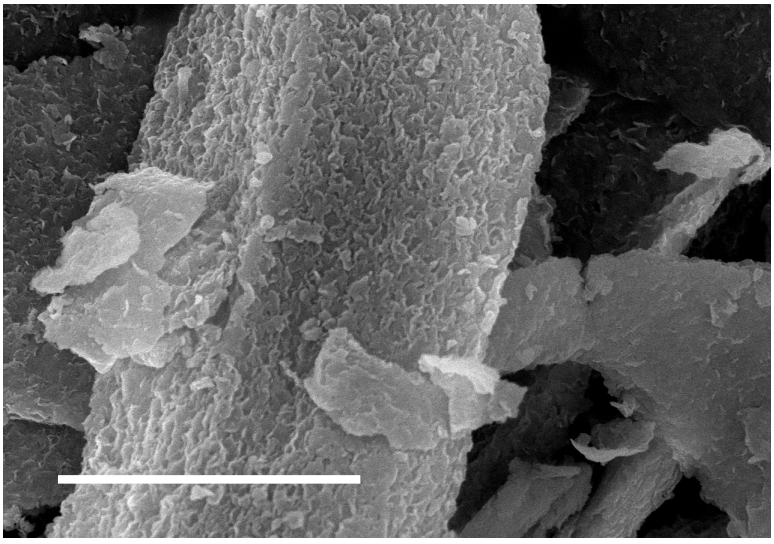

Figure S1. SEM image of C-$Ni(OH)_2$ (scale bar: (a) 1 μm and (b) 2 μm)

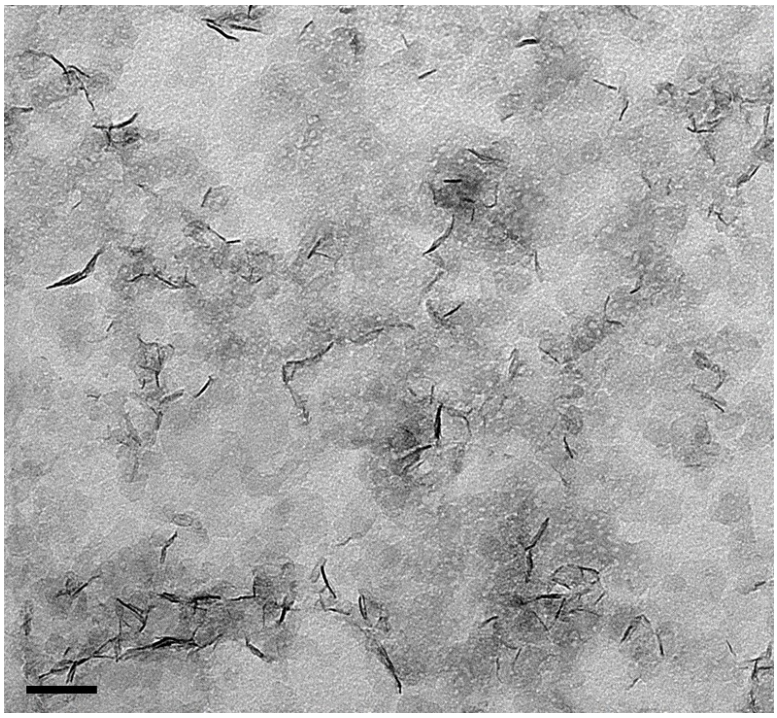

Figure S2. TEM Tecnai F20 image of A-$Ni(OH)_2$(scale bar: 50 nm)

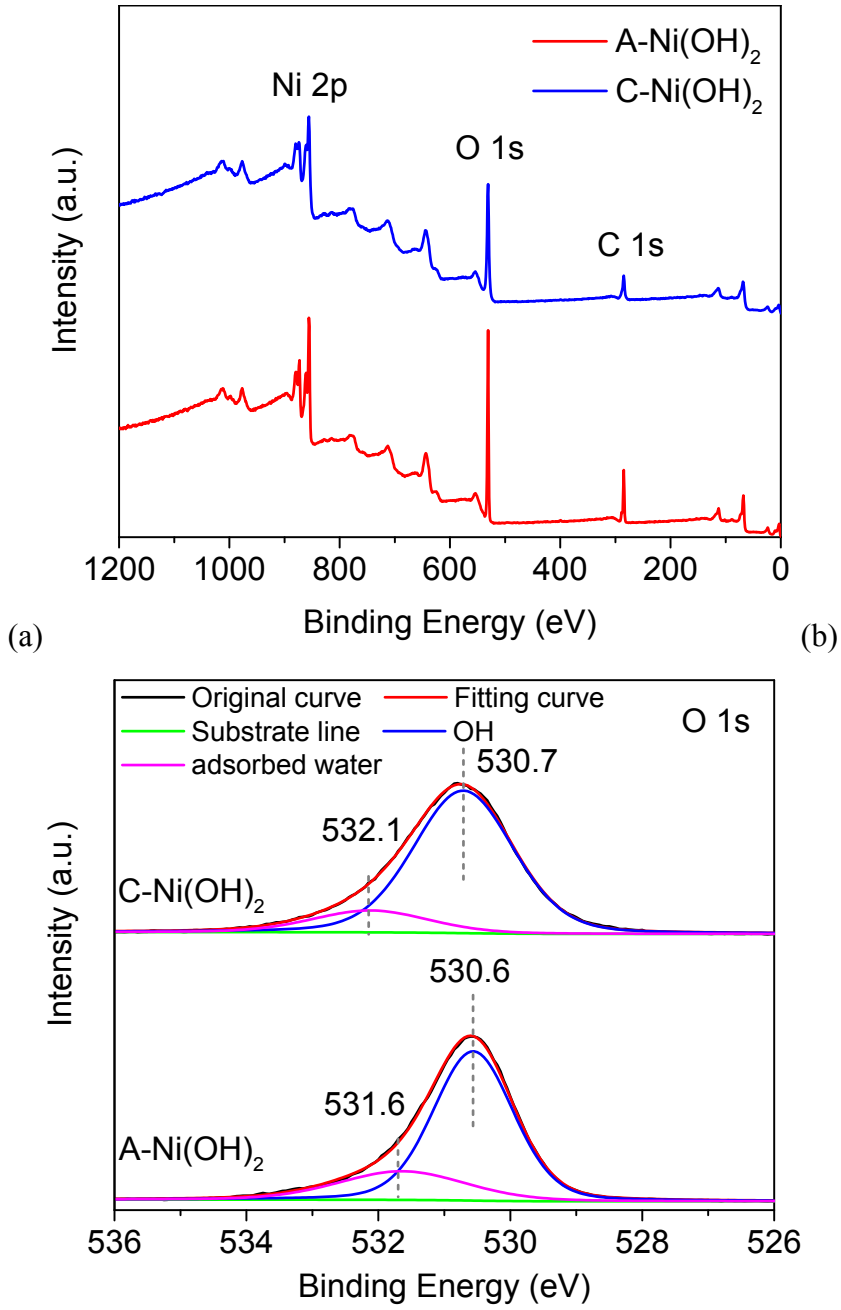

Figure S3. (a) XPS survey and (b) deconvoluted oxygen 1s spectra (b) of C-$Ni(OH)_2$ and A-$Ni(OH)_2$ in high-resolution XPS.

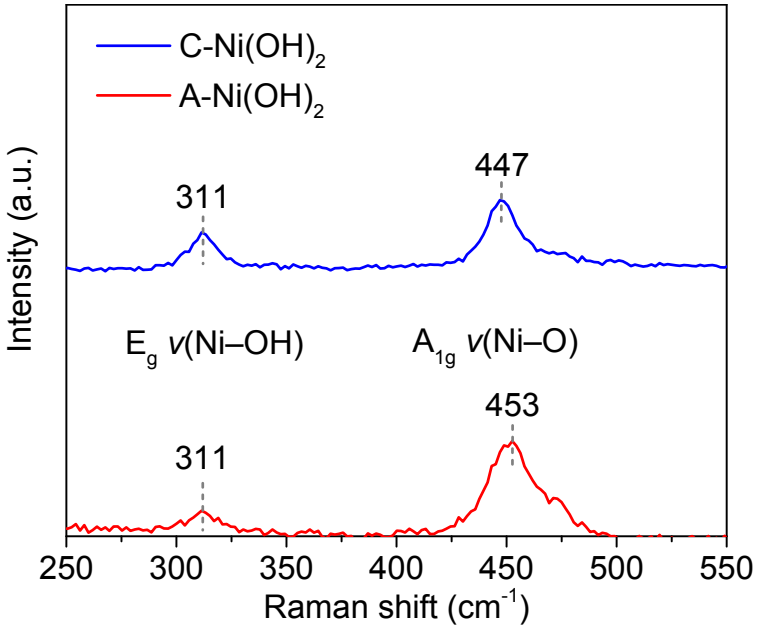

Figure S4. Partial Raman spectra of the Ni−O lattice modes of C-$Ni(OH)_2$ and A-$Ni(OH)_2$.

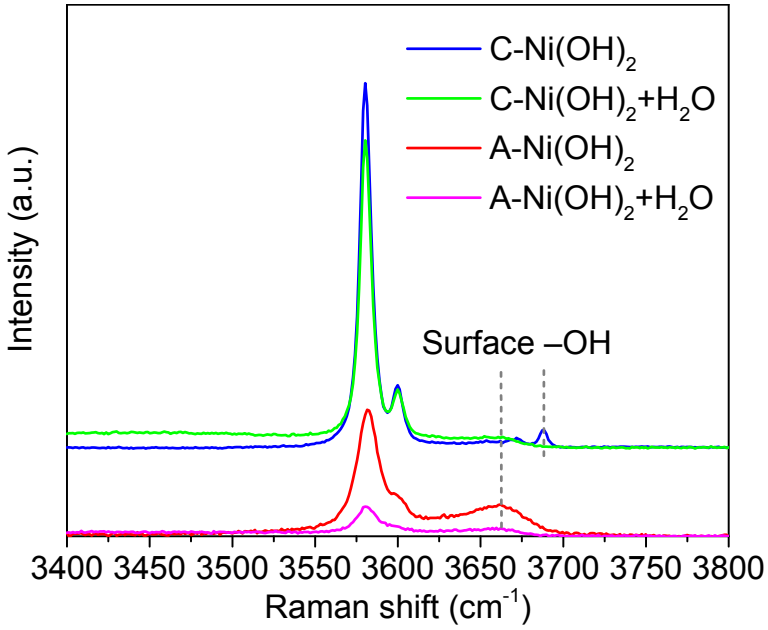

Figure S5. Effect of addition of water on the O−H stretching zone of Raman spectra of A-$Ni(OH)_2$ and C-$Ni(OH)_2$.

Note: The disappear of surface OH vibration in the Raman spectra of C-$Ni(OH)_2$ is ascribed to the hydrogen bonds between the free OH groups located on the surface of A-$Ni(OH)_2$ and water molecules. However, the intensity of the surface OH peak (~3689 cm^{-1}) in Raman spectrum of A-$Ni(OH)_2$ decreased but does not vanish completely. This result indicates that some of free OH groups on the surface of A-$Ni(OH)_2$ are not bonded with the water molecules, which might cause the significant discrepancy of the PMS activation process.

Table S1. The content of Ni ion in A-$Ni(OH)_2$ colloid samples quantified by ICP-OES before each cycle experiment

Cycle	1st	2nd	3rd	4th	5th
Ni^{2+} (mg/L)	756.2	666.1	555.3	417.0	300.1

(Acidification: HCl and HNO_3)

Note : The used A-$Ni(OH)_2$ samples after centrifugation was redispersed in DI water, then the mixture of suspension was treated by ultrasound for 30 min. It should be noted that the Ni content was determined by the volume of DI water in re-dispersion process, which may cause the loss of active component. The dosage of A-$Ni(OH)_2$ sample was kept at 0.2 g/L in every cycle experiment.

Table S2. EXAFS structural parameters for Ni foil A-$Ni(OH)_2$ and C-$Ni(OH)_2$ samples

Sample	Atomic Scatter	Coordination Number	Bond Length(Å)	Debye-Waller factor($10^{-3}\times Å^2$)	R factor
Ni foil	Ni-Ni	12	2.48±0.01	6.1±0.2	0.0003
A-$Ni(OH)_2$	Ni-O	6.2±0.4	2.06±0.01	5.4±0.7	0.004
A-$Ni(OH)_2$	Ni-Ni	6.0±0.7	3.11±0.01	6.6±0.8	0.004
C-$Ni(OH)_2$	Ni-O	5.8±0.4	2.06±0.01	5.1±0.7	0.003
C-$Ni(OH)_2$	Ni-Ni	6.0±0.7	3.11±0.01	6.5±0.8	0.003

Table S3. Comparison of the *v*-value by various catalysts for PMS activation in RhB removal.

Catalyst	Element	Pollutant (mg/L)	Removal efficiency (%)/Time (min)	PMS dosage (mg/L)	Catalysis loading (mg/L)	*v*-value (μmol s^{-1} g^{-1})	Ref.
Amorphous boron	B	10	~100(120)	153.5	200	0.014	[8]
NPC-ZIF8	N and C	20	90(60)	491.2	200	0.052	[9]
Ca-Fe_2O_3	Fe, Ca and O	10	99(120)	200	500	0.006	[10]
$FeyCo_3$-y$[Co(CN)_6]_2$	Fe, Co, C and N	15	99.7(20)	300	100	0.260	[11]
$MnFe_2O_4$-rGO	Mn, Fe, C, O	20	69.5[a](120)	500	50	0.081	[12]
α-MnO_2/Palygorskite	Mn, Mg, Al, Si, H and O	20	100(180)	100	100	0.039	[13]
MnOx-N-biochar	Mn, N, C and O	20	99.7(60)	503.5	200	0.058	[14]
$LaCoO_3$	Co, La and O	10	97.6[a](60)	100	100	0.057	[15]
Co@NC	Co, N and C	20	84.1(120)	200	20	0.244	[16]
ZIF9@GEL	Co, N and C	50	99(10)	600	600	0.287	[17]
Co-hydroxyapatite	Co, Ca, P, H and O	40	99.3(12)	122.8	200	0.576	[18]
$CoFe_2O_4$/TNTs	Fe, Co, Ti and O	100	100(30)	4000	200	0.580	[19]
Co_3O_4–Bi_2O_3	Co, Bi and O	9.58	~100(10)	153.5	50	0.667	[20]
$Co_xMn_{3-x}O_4$	Co, Mn, and O	30	100(80)	200	20	0.652	[21]
C-$Ni(OH)_2$	Ni, O and H	10	64.7(20)	150	200	0.056	This work
C-$Ni(OH)_2$	Ni, O and H	10	15.9(20)	150	50	0.055	This work
A-$Ni(OH)_2$	Ni, O and H	10	78.2(1)	150	200	1.360	This work
A-$Ni(OH)_2$	Ni, O and H	10	97.8(2.5)	150	100	1.362	This work
A-$Ni(OH)_2$	Ni, O and H	10	93.8(5)	150	50	1.306	This work

Note: Symbol "~" means the approximate value of removal efficiency in the reference. Symbol "a" means that the removal efficiency is calculated on the reaction rate constant in the paper.

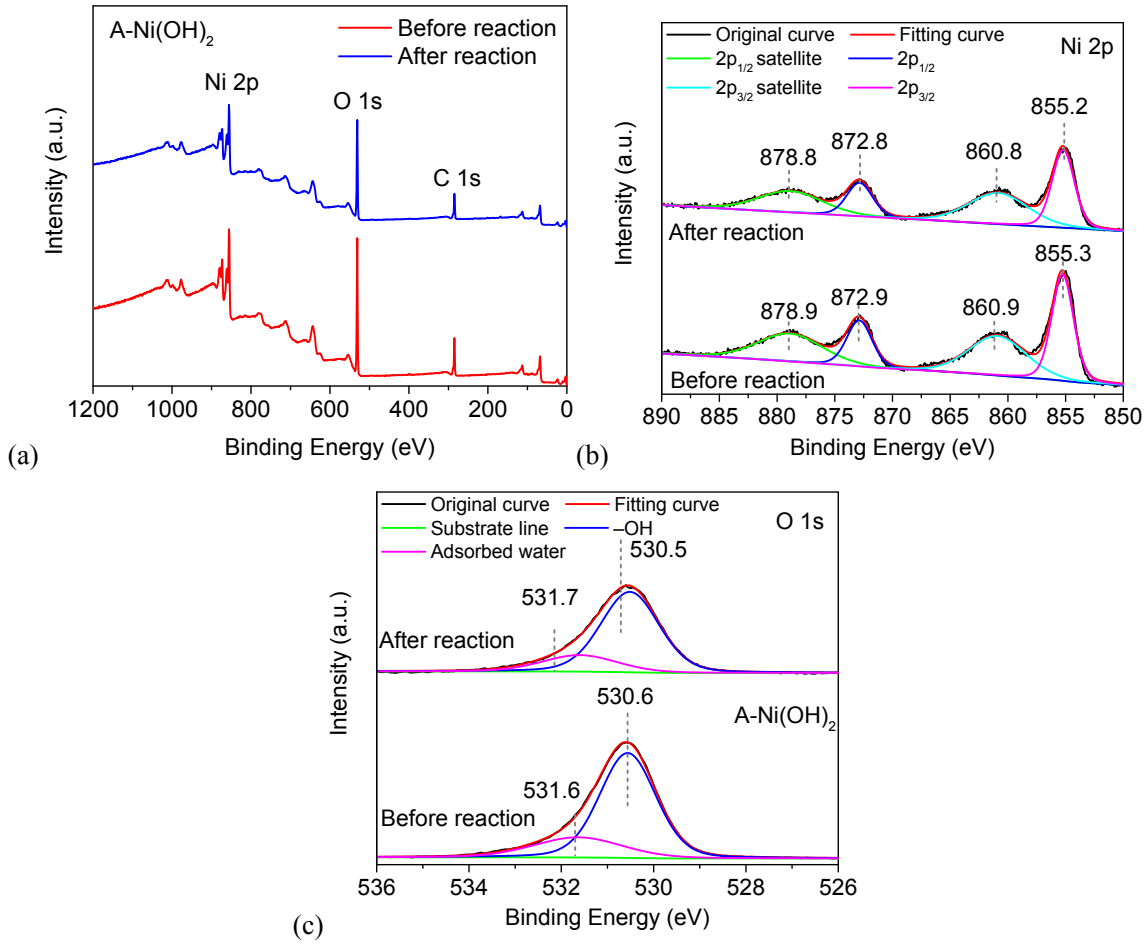

Figure S6. (a) XPS survey, (b) deconvoluted Ni 2p spectra and (c) deconvoluted oxygen 1s spectra of A-Ni(OH)$_2$ before and after activation for PMS.

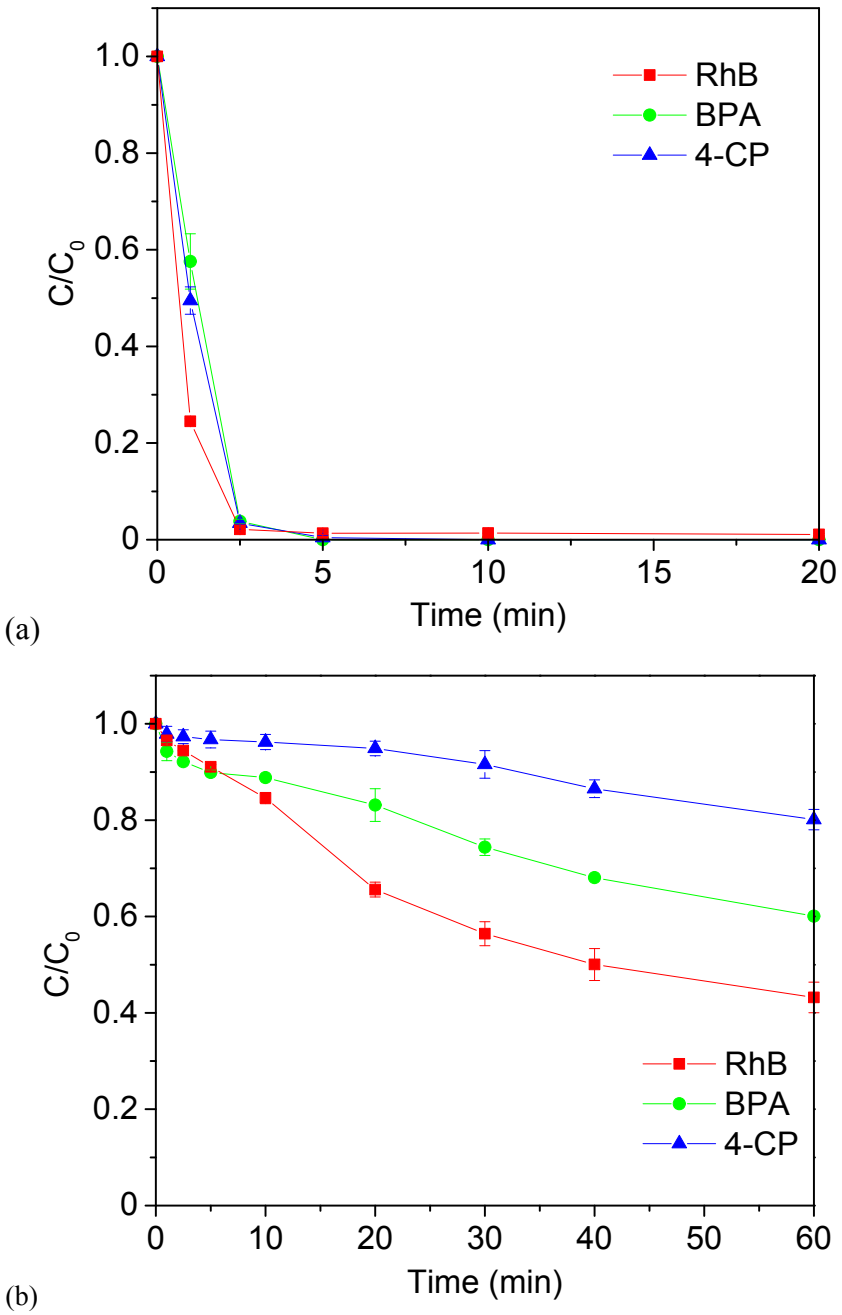

Figure S7. The evolution of RhB, BPA and 4-CP in PMS reaction systems catalyzed by (a) A-$Ni(OH)_2$ and (b) C-$Ni(OH)_2$.Reaction condition: [Organics] = 10 mg L^{-1}, [PMS] = 0.15 g L^{-1}, [Catalyst] = 0.10 g L^{-1}.

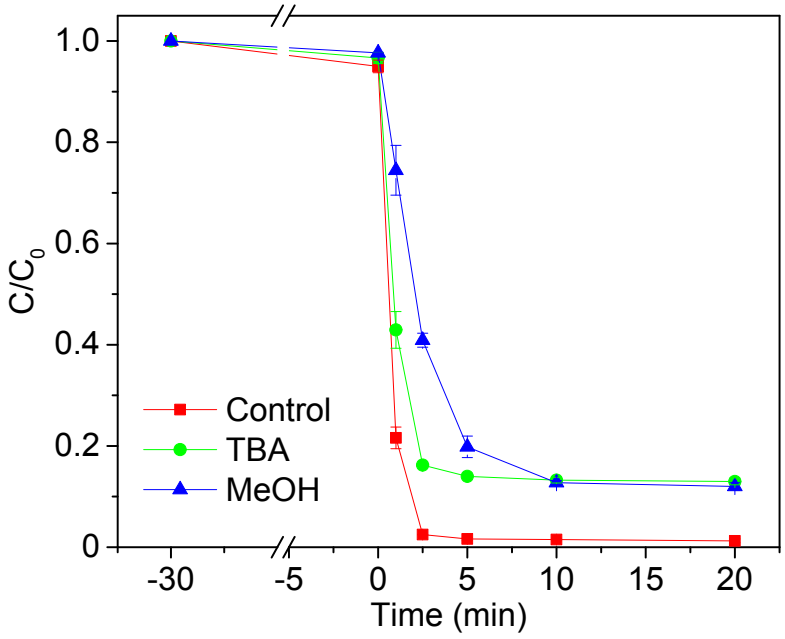

Figure S8. Degradation curves of RhB in A-$Ni(OH)_2$ and PMS system in the presence of diverse scavengers. [RhB] = 10 mg L^{-1}, [PMS] = 0.15 g L^{-1}, [Catalyst] = 0.20 g L^{-1} and [TBA] = [methanol] = 1.0 M (if needed).

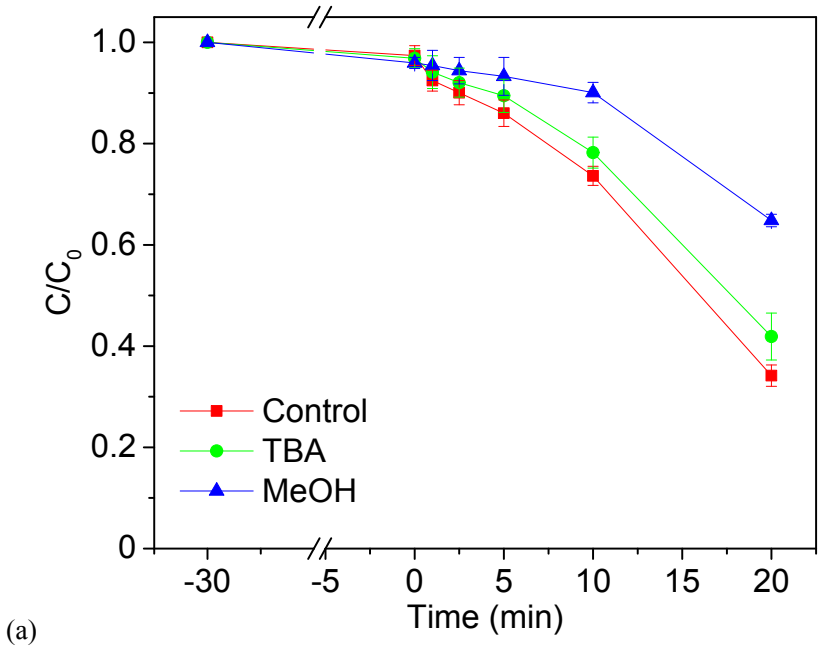

(a)

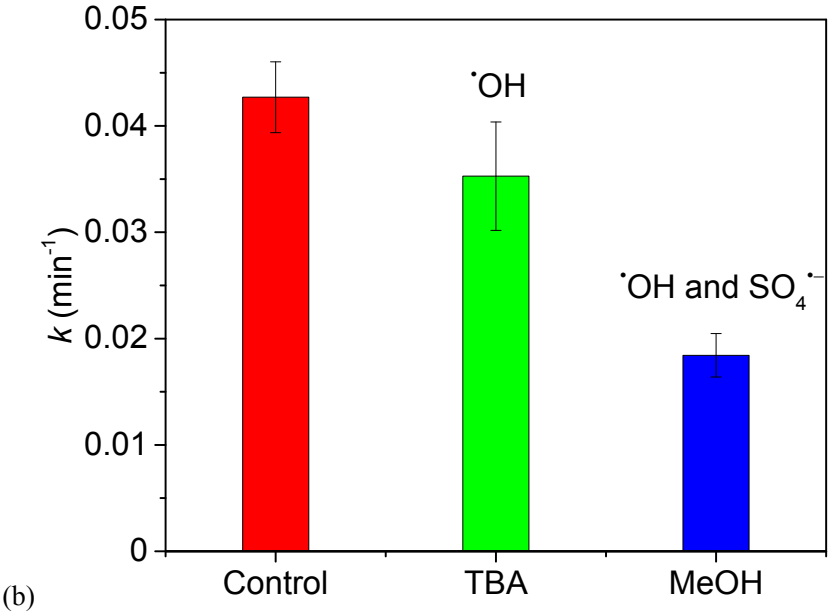

(b)

Figure S9. (a) Degradation curves of RhB in PMS and C-Ni(OH)$_2$ system in the presence of diverse scavengers. (b) Reaction rate constant of RhB Degradation in C-Ni(OH)$_2$ and PMS system in the presence of diverse scavengers. [RhB] = 10 mg L^{-1}, [PMS] = 0.15 g L^{-1}, [Catalyst] = 0.20 g L^{-1} and [TBA] = [methanol] = 1.0 M (if needed).

Note : It can be clearly found that the presence of TBA shows negligible inhibition on RhB degradation, indicating the absence of •OH in the C-Ni(OH)$_2$ PMS system.

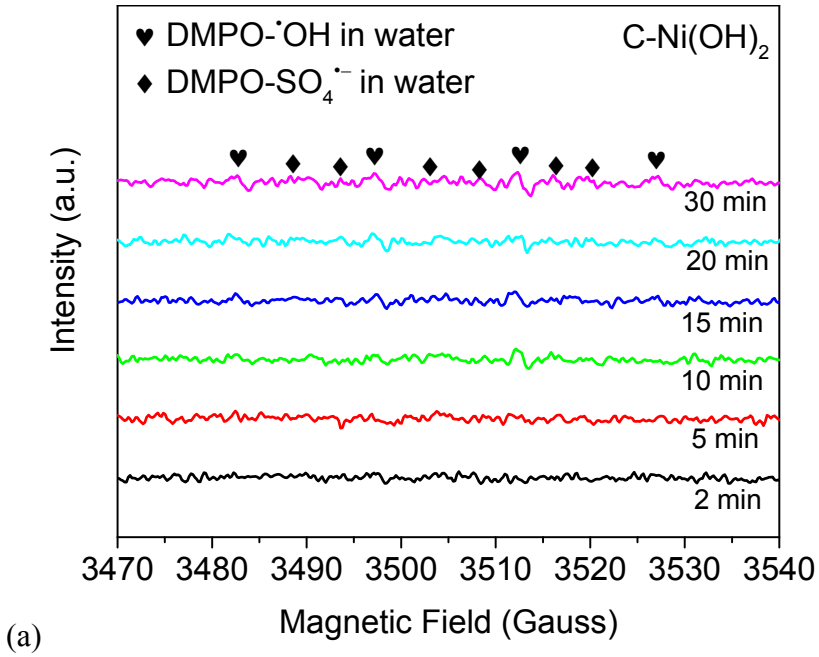

(a)

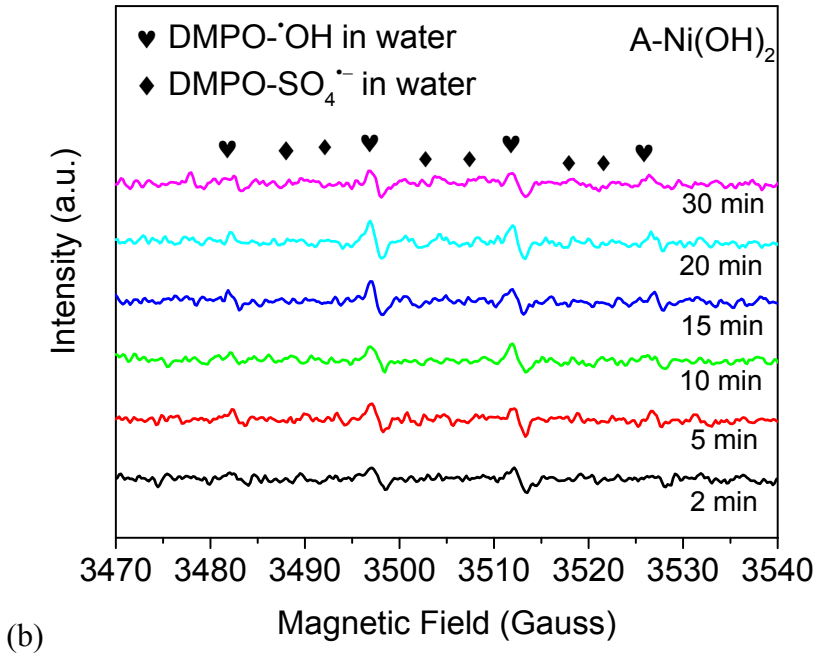

(b)

Figure S10. EPR spectra for •OH/•SO_4^- in the aqueous (a) C-$Ni(OH)_2$/PMS or (b) A-$Ni(OH)_2$/PMS system. Reaction condition: [DMPO] = 250 mM, [PMS] = 0.15 g L^{-1}, catalyst = 0.05 g L^{-1}.

Note: The pronounced difference in the peak intensities between the two counterparts attests that A-$Ni(OH)_2$ definitely gives rise to the production of •OH and $SO_4^{\bullet-}$ in the PMS activation process, which would benefit the catalytic performance.

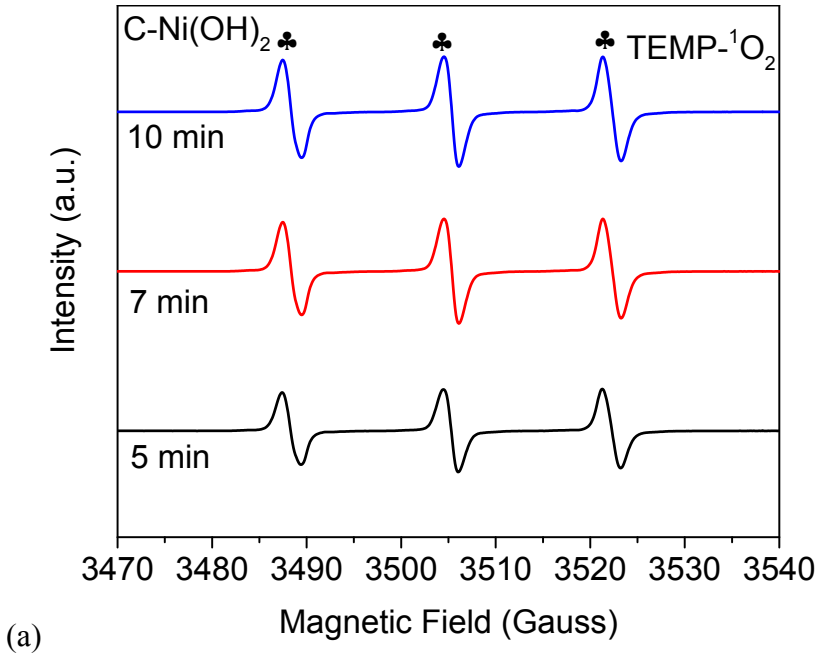

(a)

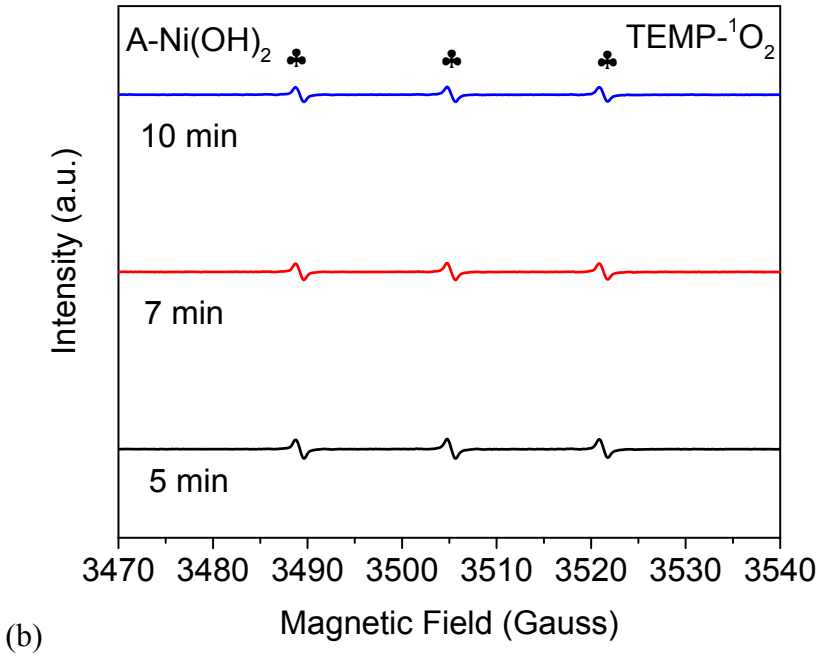

(b)

Figure S11. EPR spectra for $^1O_2$ in the (a) C-Ni(OH)$_2$/PMS or (b) A-Ni(OH)$_2$/PMS system. Reaction condition: [TEMP] = 100 mM, [PMS] = 0.15 g L^{-1}, catalyst = 0.20 g L^{-1}.

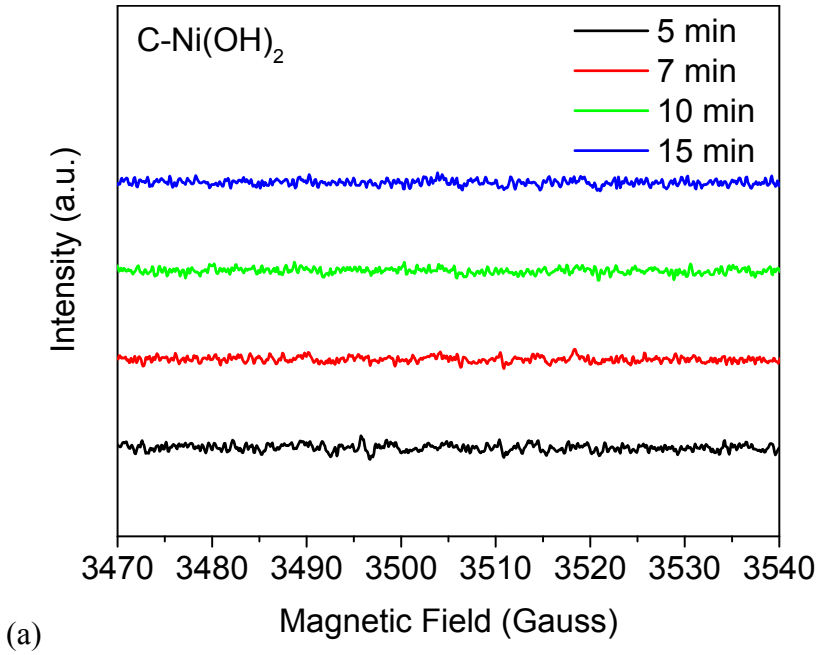

(a)

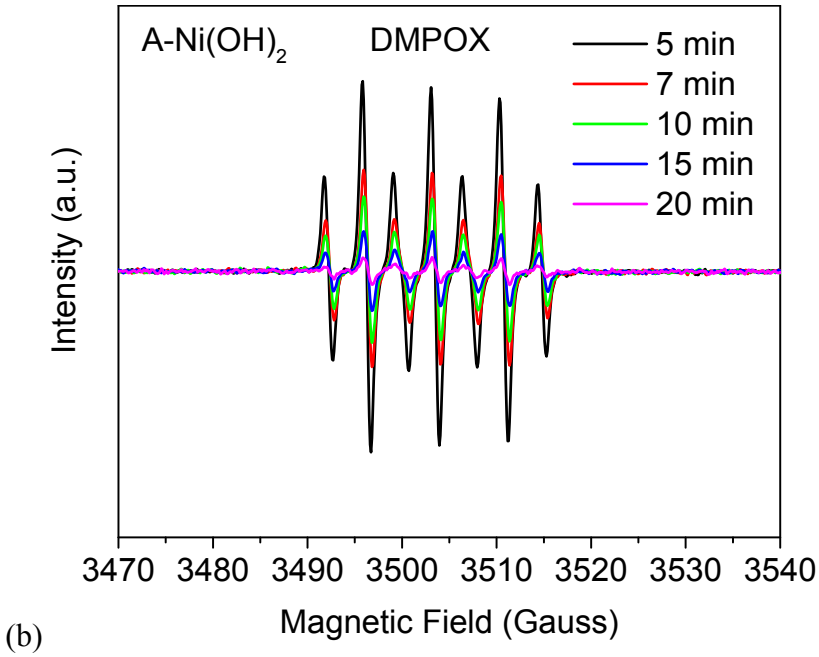

(b)

Figure S12. EPR spectra for DMPOX in the aqueous (a) C-$Ni(OH)_2$/PMS or (b) A-$Ni(OH)_2$/PMS system. Reaction condition: [DMPO] = 250 mM, [PMS] = 0.15 g L^{-1}, catalyst = 0.20 g L^{-1}.

Note. The DMPOX signals were detected in A-$Ni(OH)_2$/PMS system and no signal was found in C-$Ni(OH)_2$/PMS system when the dosage of catalyst was increased to 0.20 g L^{-1}. The free radicals were not trapped by the spin trap DMPO, but the DMPO molecular

was oxidized itself, demonstrating that the strong oxidative ability from A-$Ni(OH)_2$/PMS system. This phenomenon depends on the ratio between catalyst, oxidant and DMPO. Since the DMPOX would not be formed from the reaction between $^1O_2$ (detected in C-$Ni(OH)_2$/PMS system in **Figure S11**) and DMPO, the DMPO molecular was most likely to be oxidized by $^{\bullet}OH$ or/and $SO_4^{\bullet-}$ radicals.

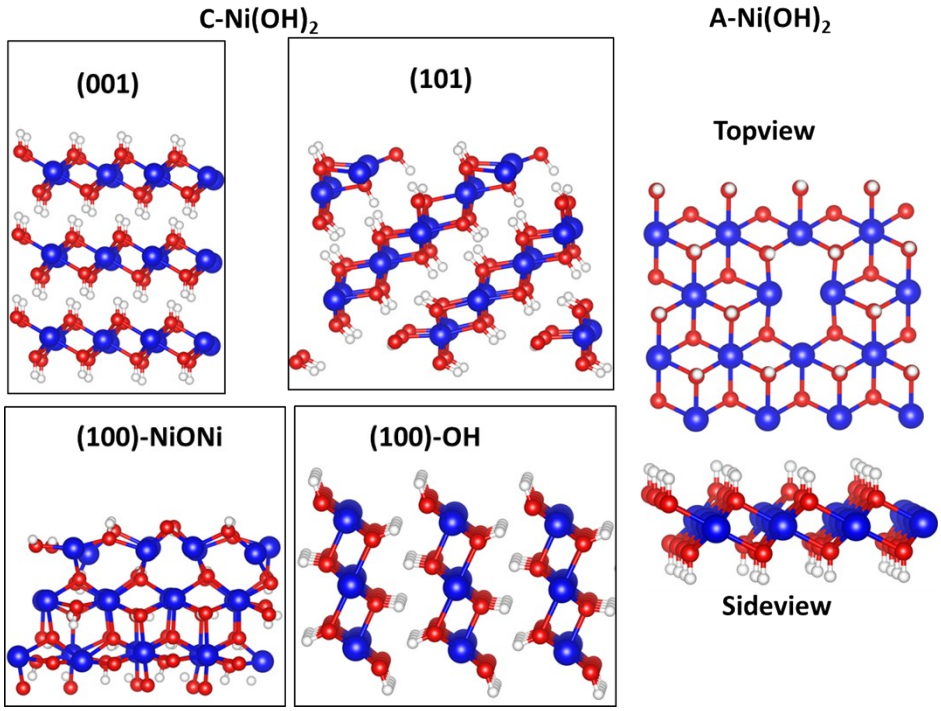

Figure S13. The simulated surface structures of C-$Ni(OH)_2$ (001), (101), NiONi-terminated (100), OH-terminated (100), and topview and sideview structures of disordered A-$Ni(OH)_2$.

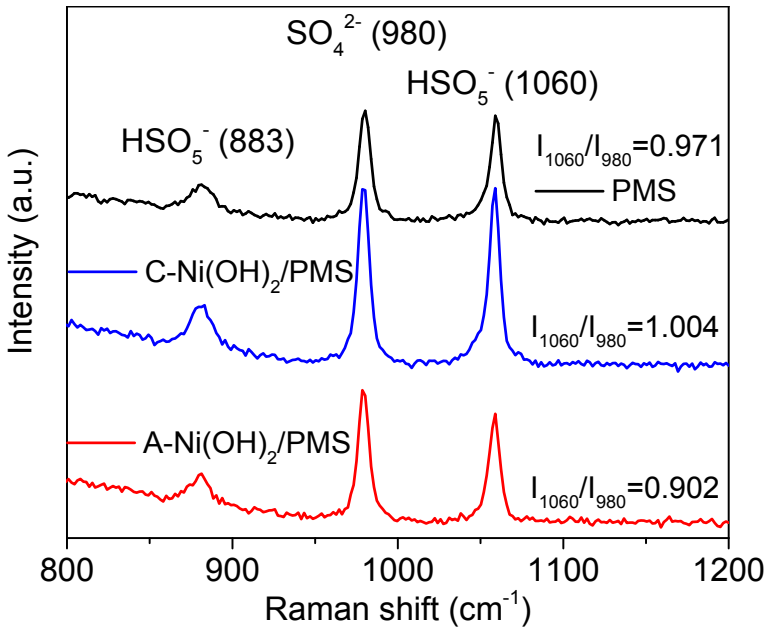

Figure S14. In-situ Raman spectra of PMS, A-$Ni(OH)_2$/PMS and C-$Ni(OH)_2$/PMS system in 2 min.

Note: The ratio I_{1060}/I_{980} was decreased to 0.902 in A-$Ni(OH)_2$/PMS system the compared to that of pure PMS, indicating that the transformation from HSO_5^- to SO_4^{2-} highly accelerated. This result manifests the faster PMS consumption in A-$Ni(OH)_2$/PMS system, which exhibited the catalytic ability of A-$Ni(OH)_2$.

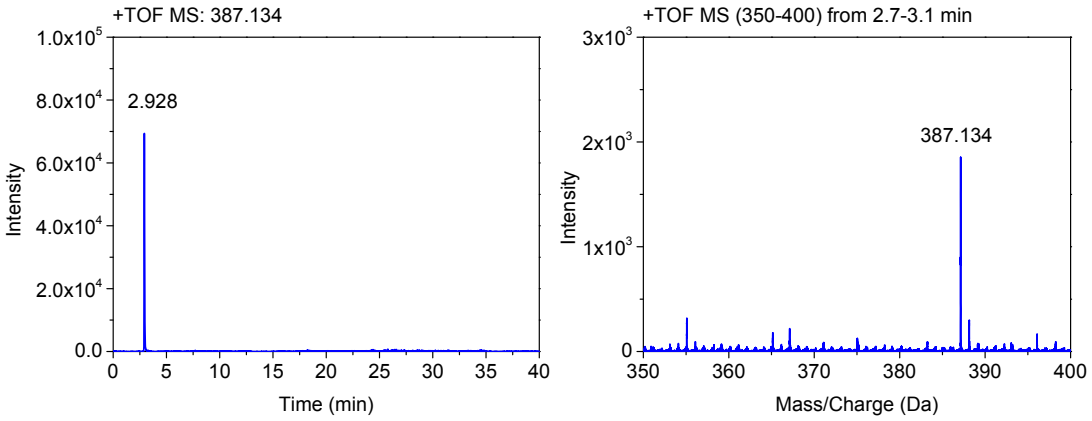

(a)

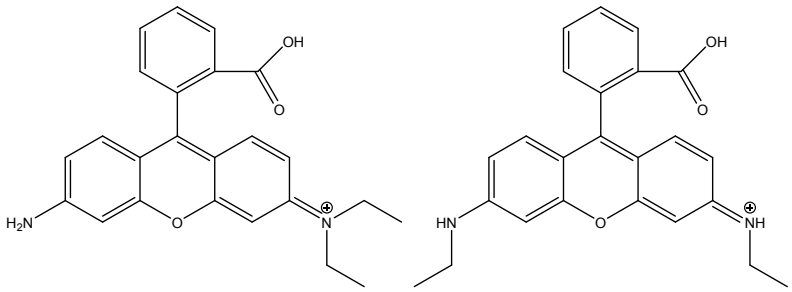

m/z 387.170

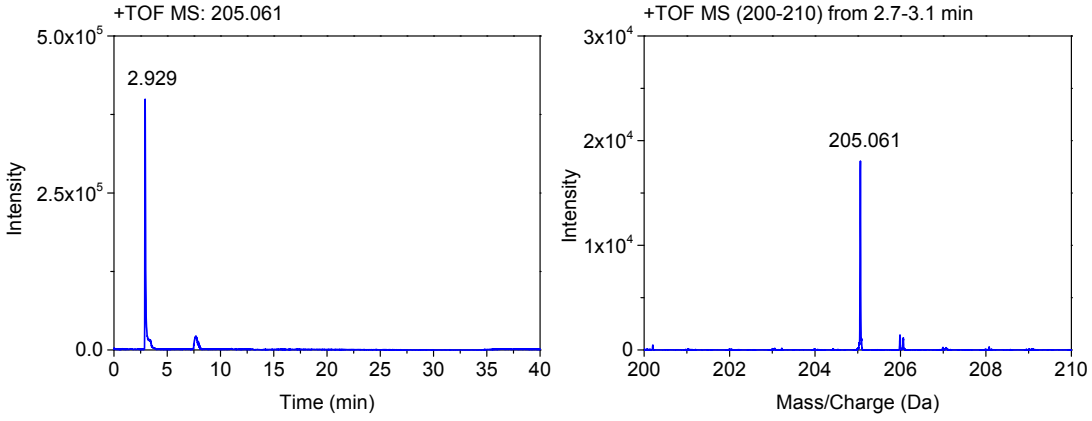

(b)

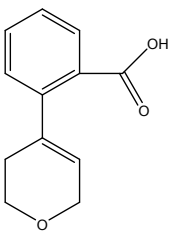

m/z 205.086 $[M+H]^+$

Figure S15. MS spectra of intermediate product in the A-Ni$(OH)_2$/PMS system detected by QTOF/MS/MS: (a) bisDERhB and (b) P-204.

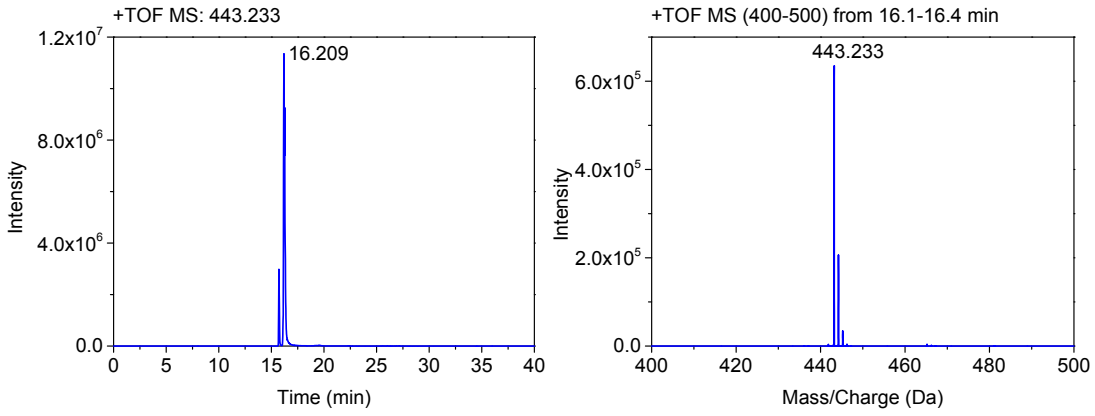

(a)

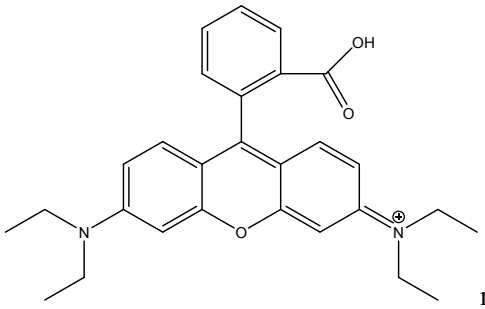

m/z 443.233 RhB

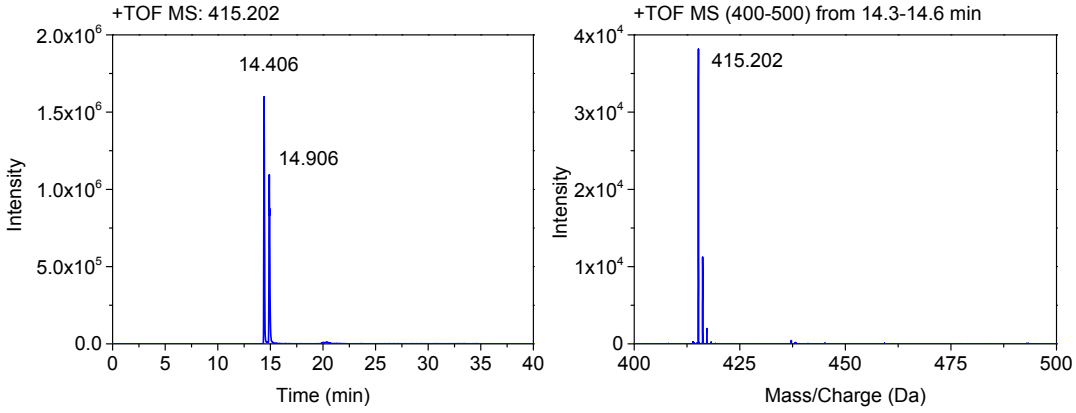

(b)

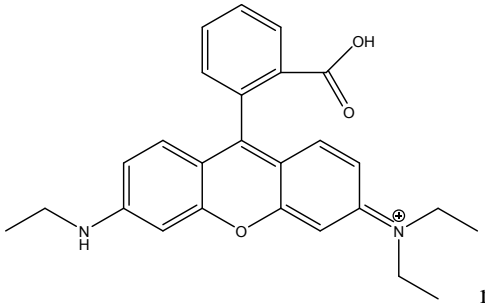

m/z 415.201

(c)

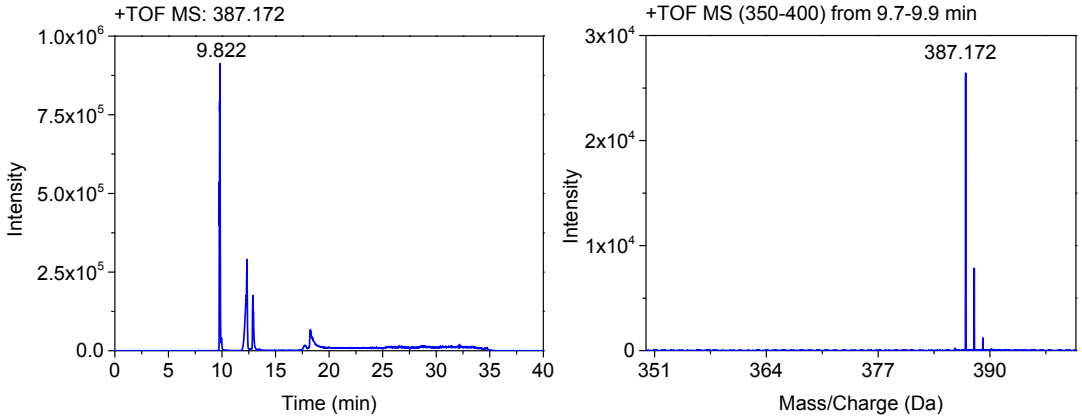

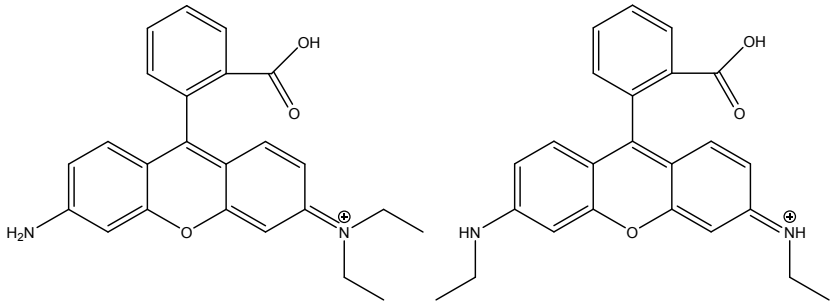

m/z 387.170

(d)

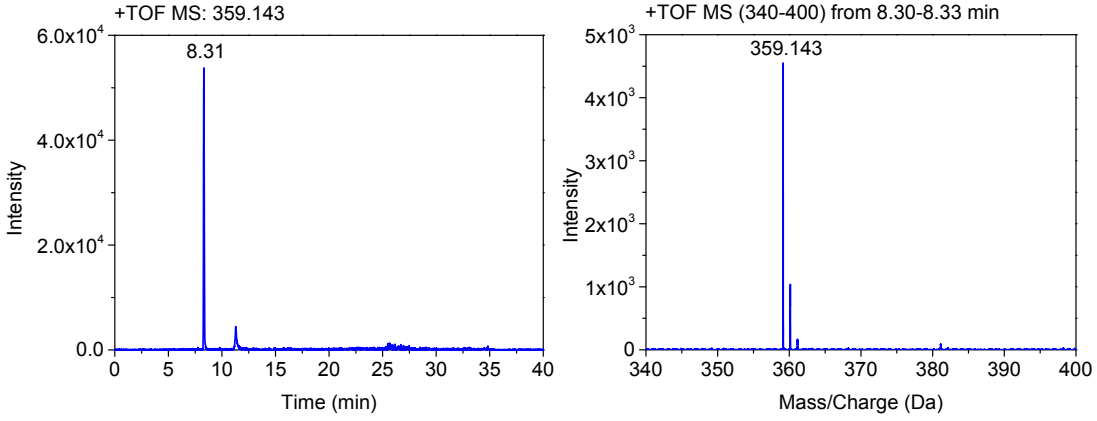

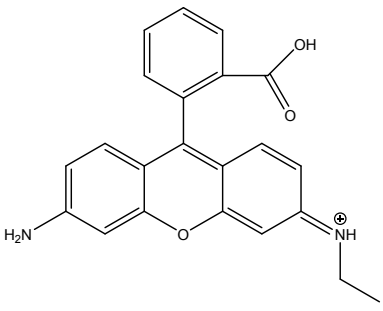

m/z 359.139

(e)

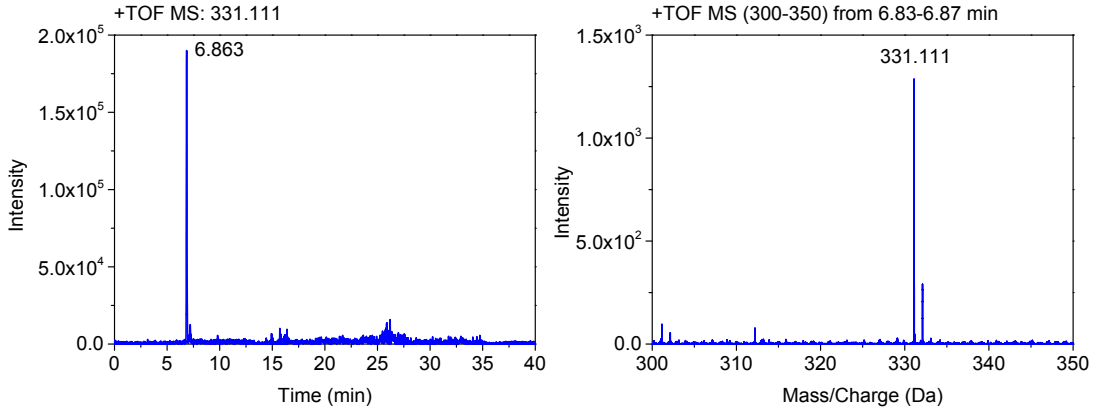

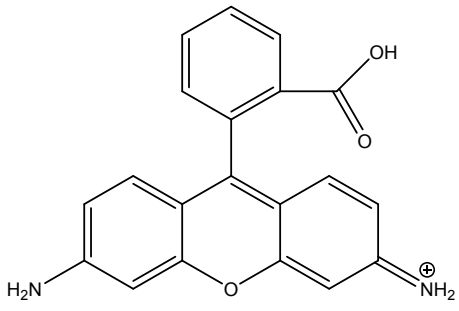

m/z 331.108

(f)

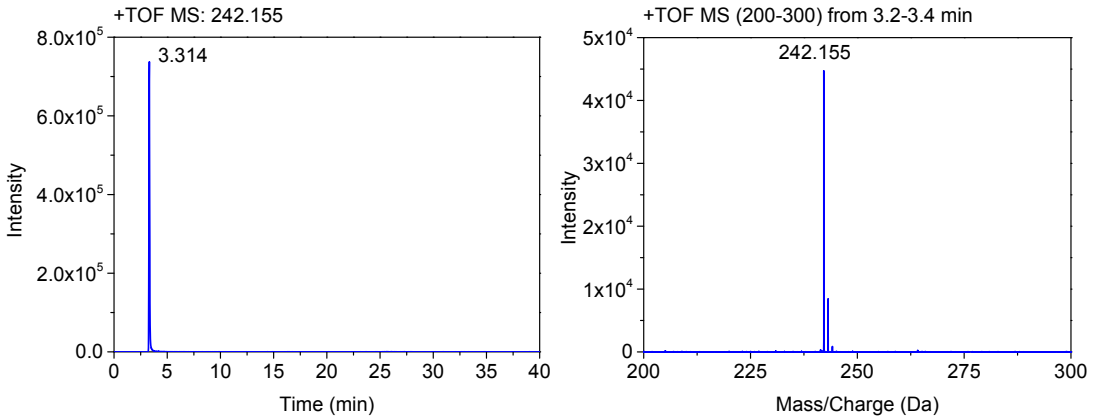

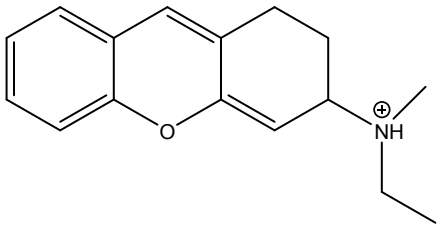

m/z 242.154

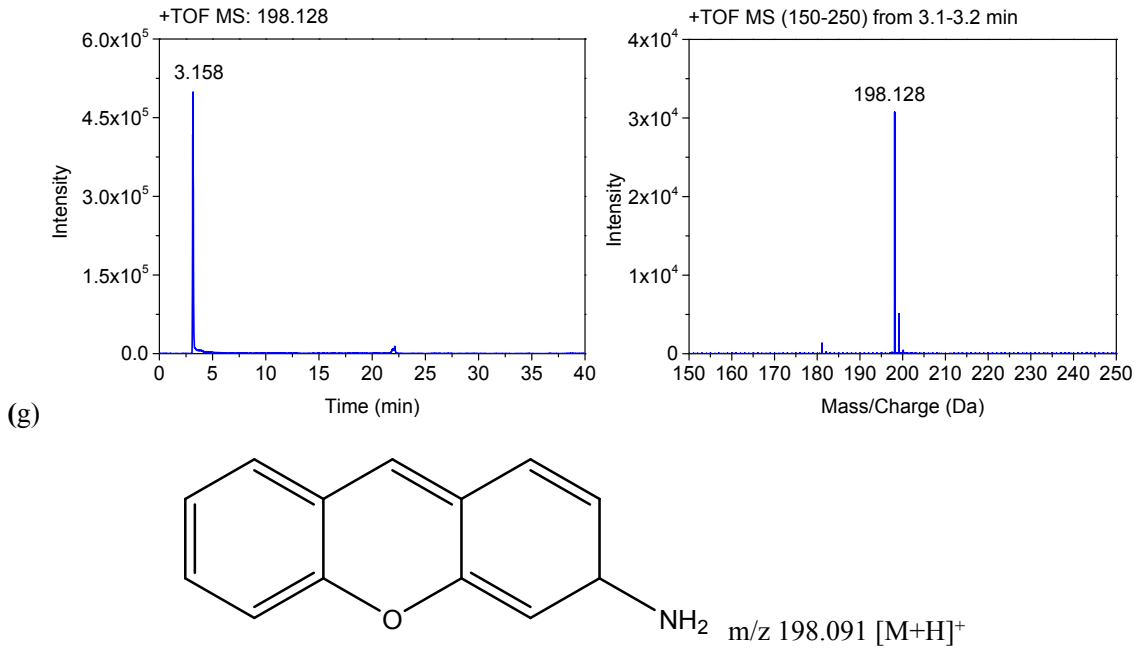

Figure S16. MS spectra of intermediate product in the C-Ni$(OH)_2$/PMS system detected by QTOF/MS/MS: (a) RhB, (b) DERhB, (c) bisDERhB, (d) TrisDERHB, (e) Rh, (f) P-242 and (g) P-197.

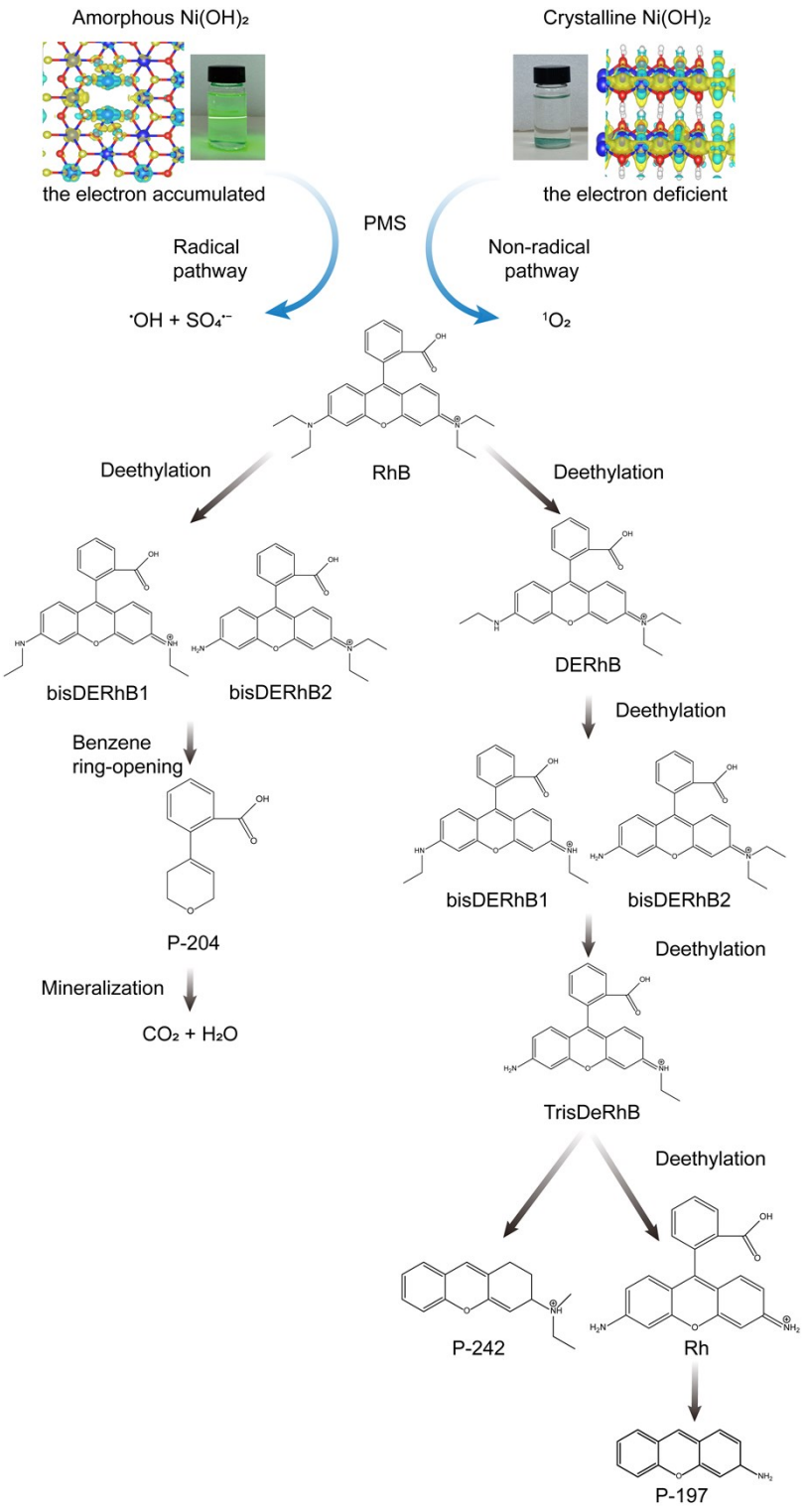

Figure S17. Schematic illustration of the catalytic mechanism and possible degradation pathway of Rhodamine B in the A-$Ni(OH)_2$ and C-$Ni(OH)_2$/PMS system.

Note : It was clearly illustrated that the degradation pathway of RhB was different

between the A-$Ni(OH)_2$/PMS and C-$Ni(OH)_2$/PMS system **(Figure S15 and S16)**, ascribed to the difference of the activity and selectivity of reactive oxygen species ($^{\bullet}OH$ and $SO_4^{\bullet-}$ *vs.* $^1O_2$) towards RhB in **Figure S17**. The intermediate product of 387 Da molecular weight was generated by de-ethylation phenomenon in the A-$Ni(OH)_2$ activated PMS process. Then, product 204 (P-204: 2-(3,6-Dihydro-2H-pyran-4-yl)benzoic acid) was formed by the benzene ring-opening, attributed to the attack of the reactive radicals. Less benzene ring and more mineralization rate meant less hazardous.[22, 23]

The RhB molecular was still detected in the C-$Ni(OH)_2$ activated PMS process because of relatively low activity of $^1O_2$ through the non-radical pathway. The consecutive losses of C_2H_4 were registered for DERhB, bisDERhB, TrisDERHB and Rh. Afterwards, the bond between xanthene group and phenyl group and the amino could be broken, as the organic intermediates were produced (m/z 242 and 197). This case study demonstrated that the transformation from non-radical to radical pathway allowed PMS activation to produce the more radicals, boosting mineralization process of organics by the breakage of benzene ring.

Author Contributions

H. Wang, L. J. Zhang, Q. J. Zhang and Z. Y. Lu designed research; H. Wang, W. W. Xu, and B. S. Zhang, J. Sun and L. J. Zhang performed research; H. Wang, W. W. Xu, X. Chen, Q. H. Yang, Y. C. Lin, Z. Y. Lu. contributed to new reagents/analytic tools; H. Wang W. W. Xu, B. S. Zhang, C. Shen, and Z. Y. Lu. and L. Chen analyzed data; and H. Wang, Q. J. Zhang and Z. Y. Lu. wrote the paper.

Reference:

1 B. Ravel and M. Newville, *J Synchrotron Radiat*, 2005, **12**, 537-541.

2 S. Grimme, *J. Comput. Chem. Mater.*, 2006, **27**, 1787-1799.

3 G. Kresse and J. Furthmuller, *Phys. Rev. B*, 1996, **54**, 11169-11186.

4 P.E.Blochl, *Phys. Rev. B*, 1994, **50**, 50-76.

5 J. P. Perdew and Y. Wang, *Phys. Rev. B: Condens. Matter* 1992, **46**, 12947-12954.

6 H. J, Monkhorst and J. D.Pack, *Phys. Rev. B*, 1976, **13**, 5188-5192.

7 I. Morrison, J. C. Li, S. Jenkins, S. S. Xantheas and M. C. Payne, *J. Phys. Chem. B*, 1997, **101**, 6146-6150.

8 P. Shao, X. Duan, J. Xu, J. Tian, W. Shi, S. Gao, M. Xu, F. Cui and S. Wang, *J. Hazard. Mater.*, 2017, **322**, 532-539.

9 G. Wang, S. Chen, X. Quan, H. Yu and Y. Zhang, *Carbon*, 2017, **115**, 730-739.

10 S. Guo, H. J. Wang, W. Yang, H. Fida, L. M. You and K. Zhou, *Appl. Catal., B*, 2020, **262**, 118250.

11 L. Zeng, L. Xiao, X. Shi, M. Wei, J. Cao and Y. Long, *J. Colloid Interf. Sci.*, 2019, **534**, 586-594.

12 Y. Yao, Y. Cai, F. Lu, F. Wei, X. Wang and S. Wang, *J. Hazard. Mater.*, 2014, **270**, 61-70.

13 C. Huang, Y. Wang, M. Gong, W. Wang, Y. Mu and Z. H. Hu, *Sep. Purif. Technol.*, 2020, **230**, 115877.

14 M. M. Mian, G. J. Liu, B. Fu and Y. Song, *Appl. Catal., B*, 2019, **255**, 117765.

15 K.-Y. A. Lin, Y.-C. Chen and Y.-F. Lin, *Chem. Eng. Sci.*, 2017, **160**, 96-105.

16 Y. Yao, H. Chen, C. Lian, F. Wei, D. Zhang, G. Wu, B. Chen and S. Wang, *J. Hazard. Mater.*, 2016, **314**, 129-139.

17 W. Ren, J. Gao, C. Lei, Y. Xie, Y. Cai, Q. Ni and J. Yao, *Chem. Eng. J.*, 2018, **349**, 766-774.

18 Y. Pang, L. Kong, D. Chen, G. Yuvaraja and S. Mehmood, *J. Hazard. Mater.*, 2020, **384**, 121447.

19 Y. Du, W. Ma, P. Liu, B. Zou and J. Ma, *J. Hazard. Mater.*, 2016, **308**, 58-66.

20 Y. B. Ding, L. H. Zhu, A. Z. Huang, X. R. Zhao, X. Y. Zhang and H. Q. Tang, *Catal. Sci. Technol.*, 2012, **2**, 1977-1984.

21 Y. Yao, Y. Cai, G. Wu, F. Wei, X. Li, H. Chen and S. Wang, *J. Hazard. Mater.*, 2015, **296**, 128-137.

22 H. Ha, K. Park, G. Kang and S. Lee, *Ecotoxicology*, 2019, **28**, 333-342.

23 B. Korchowiec, Y. Corvis, T. Viitala, C. Feidt, Y. Guiavarch, C. Corbier and E. Rogalska, *J. Phys. Chem. B*, 2008, **112**, 13518-13531.